The ability to naturally integrate state-of-the-art electronic materials and devices represents an essential, defining characteristic of these approaches. A mechanically tunable inductor based on a 3D toroidal structure with feed and ground lines, all constructed with polyimide encapsulation (1.2 μm) and Ni conducting layers (400 nm), provides an example. Here, the geometry is similar to the "circular helix III" in Fig. 2D, with the addition of contact pads located at the periphery for electrical probing. The graph of Fig. 4D shows measurements and modeling results for the frequency dependence of the inductance and the quality (Q) factor for a 2D closed-loop serpentine precursor and a single 3D toroid structure in two different mechanically adjusted configurations. In both cases, the 3D cage structure enhances the mutual inductance between adjacent twisted turns. The maximum Q factors and resonant frequencies increase systematically from 1.7 to 2.2 GHz and from 6.8 to 9.5 GHz, respectively, as the structure transforms from 2D to two distinct 3D shapes associated with partial release (about half of the total initial prestrain of 54%) and then complete release of the prestrain. These trends arise from a systematic reduction in substrate parasitic capacitance with increasing three-dimensional character (*40*). The measured results correspond well to modeling that involves computation of the electromagnetic properties associated with the predicted 3D structure geometries from FEA, as shown in the right panels of Fig. 4D [see (*33*) and figs. S20 to S23].

The ideas presented here combine precise, lithographic control of the thicknesses, widths, and layouts of 2D structures with patterned sites of adhesion to the surfaces of high-elongation elastomer substrates to enable rapid assembly of broad classes of 3D mesostructures of relevance to diverse microsystem technologies. The process, which can be implemented with any substrate that is capable of controlled, large-scale dimensional change, expands and complements the capabilities of other approaches in 3D materials assembly. Compatibility with the most advanced materials (e.g., monocrystalline inorganics), fabrication methods (e.g., photolithography), and processing techniques (e.g., etching, deposition) that are available in the semiconductor and photonics industries suggest many possibilities for achieving sophisticated classes of 3D electronic, optoelectronic, and electromagnetic devices.

REFERENCES AND NOTES

1. V. B. Shenoy, D. H. Gracias, *MRS Bull.* **37**, 847–854 (2012).
2. F. Li, D. P. Josephson, A. Stein, *Angew. Chem. Int. Ed.* **50**, 360–388 (2011).
3. N. B. Crane, O. Onen, J. Carballo, Q. Ni, R. Guldiken, *Microfluid. Nanofluid.* **14**, 383–419 (2013).
4. J. H. Jang *et al.*, *Adv. Funct. Mater.* **17**, 3027–3041 (2007).
5. J. Fischer, M. Wegener, *Laser Photonics Rev.* **7**, 22–44 (2013).
6. K. A. Arpin *et al.*, *Adv. Mater.* **22**, 1084–1101 (2010).
7. W. L. Noorduin, A. Grinthal, L. Mahadevan, J. Aizenberg, *Science* **340**, 832–837 (2013).
8. P. X. Gao *et al.*, *Science* **309**, 1700–1704 (2005).
9. M. Huang, F. Cavallo, F. Liu, M. G. Lagally, *Nanoscale* **3**, 96–120 (2011).
10. B. Tian *et al.*, *Nat. Mater.* **11**, 986–994 (2012).
11. T. G. Leong *et al.*, *Proc. Natl. Acad. Sci. U.S.A.* **106**, 703–708 (2009).
12. M. Yu *et al.*, *ACS Nano* **5**, 2447–2457 (2011).
13. D. Bishop, F. Pardo, C. Bolle, R. Giles, V. Aksyuk, *J. Low Temp. Phys.* **169**, 386–399 (2012).
14. R. J. Wood, *Am. Sci.* **102**, 124–131 (2014).
15. R. Songmuang, A. Rastelli, S. Mendach, O. G. Schmidt, *Appl. Phys. Lett.* **90**, 091905 (2007).
16. J. H. Lee *et al.*, *Adv. Mater.* **26**, 532–569 (2014).
17. M. Schumann, T. Buckmann, N. Gruhler, M. Wegener, W. Pernice, *Light Sci. Appl.* **3**, e175 (2014).
18. X. Zheng *et al.*, *Science* **344**, 1373–1377 (2014).
19. T. A. Schaedler *et al.*, *Science* **334**, 962–965 (2011).
20. C. M. Soukoulis, M. Wegener, *Nat. Photonics* **5**, 523–530 (2011).
21. J. H. Cho *et al.*, *Small* **7**, 1943–1948 (2011).
22. B. Y. Ahn *et al.*, *Science* **323**, 1590–1593 (2009).
23. W. Huang *et al.*, *Nano Lett.* **12**, 6283–6288 (2012).
24. H. Zhang, X. Yu, P. V. Braun, *Nat. Nanotechnol.* **6**, 277–281 (2011).
25. K. Sun *et al.*, *Adv. Mater.* **25**, 4539–4543 (2013).
26. W. Zheng, H. O. Jacobs, *Adv. Funct. Mater.* **15**, 732–738 (2005).
27. X. Guo *et al.*, *Proc. Natl. Acad. Sci. U.S.A.* **106**, 20149–20154 (2009).
28. V. Y. Prinz *et al.*, *Physica E* **6**, 828–831 (2000).
29. O. G. Schmidt, K. Eberl, *Nature* **410**, 168–168 (2001).
30. L. Zhang *et al.*, *Microelectron. Eng.* **83**, 1237–1240 (2006).
31. G. Hwang *et al.*, *Nano Lett.* **9**, 554–561 (2009).
32. W. Gao *et al.*, *Nano Lett.* **14**, 305–310 (2014).
33. See supplementary materials on *Science* Online.
34. D. C. Duffy, J. C. McDonald, O. J. A. Schueller, G. M. Whitesides, *Anal. Chem.* **70**, 4974–4984 (1998).
35. Y. Sun, W. M. Choi, H. Jiang, Y. Y. Huang, J. A. Rogers, *Nat. Nanotechnol.* **1**, 201–207 (2006).
36. D. H. Kim *et al.*, *Science* **333**, 838–843 (2011).
37. S. Yang, K. Khare, P. C. Lin, *Adv. Funct. Mater.* **20**, 2550–2564 (2010).
38. S. Singamaneni, V. V. Tsukruk, *Soft Matter* **6**, 5681–5692 (2010).
39. D. H. Kim, N. S. Lu, Y. G. Huang, J. A. Rogers, *MRS Bull.* **37**, 226–235 (2012).
40. C. P. Yue, S. S. Wong, *IEEE Trans. Electron. Dev.* **47**, 560–568 (2000).

ACKNOWLEDGMENTS

Supported by the U.S. Department of Energy, Office of Science, Basic Energy Sciences, under award DE-FG02-07ER46741. We thank S. B. Gong for providing the RF testing equipment in this study, and K. W. Nan, H. Z. Si, J. Mabon, J. H. Lee, Y. M. Song, and S. Xiang for technical support and stimulating discussions. Full data are in the supplementary materials.

SUPPLEMENTARY MATERIALS

www.sciencemag.org/content/347/6218/154/suppl/DC1
Materials and Methods
Supplementary Text
Figs. S1 to S23

7 September 2014; accepted 17 November 2014
10.1126/science.1260960

BIOMATERIALS

Electronic dura mater for long-term multimodal neural interfaces

Ivan R. Minev,[1]* Pavel Musienko,[2,3]* Arthur Hirsch,[1] Quentin Barraud,[2] Nikolaus Wenger,[2] Eduardo Martin Moraud,[4] Jérôme Gandar,[2] Marco Capogrosso,[4] Tomislav Milekovic,[2] Léonie Asboth,[2] Rafael Fajardo Torres,[2] Nicolas Vachicouras,[1,2] Qihan Liu,[5] Natalia Pavlova,[2,3] Simone Duis,[2] Alexandre Larmagnac,[6] Janos Vörös,[6] Silvestro Micera,[4,7] Zhigang Suo,[5] Grégoire Courtine,[2]†‡ Stéphanie P. Lacour[1]†‡

The mechanical mismatch between soft neural tissues and stiff neural implants hinders the long-term performance of implantable neuroprostheses. Here, we designed and fabricated soft neural implants with the shape and elasticity of dura mater, the protective membrane of the brain and spinal cord. The electronic dura mater, which we call e-dura, embeds interconnects, electrodes, and chemotrodes that sustain millions of mechanical stretch cycles, electrical stimulation pulses, and chemical injections. These integrated modalities enable multiple neuroprosthetic applications. The soft implants extracted cortical states in freely behaving animals for brain-machine interface and delivered electrochemical spinal neuromodulation that restored locomotion after paralyzing spinal cord injury.

Implantable neuroprostheses are engineered systems designed to study and treat the injured nervous system. Cochlear implants restore hearing in deaf children, deep brain stimulation alleviates Parkinsonian symptoms, and spinal cord neuromodulation attenuates chronic neuropathic pain (*1*). New methods for recording and modulation of neural activity using electrical, chemical, and/or optical modalities open promising therapeutic perspectives for neuroprosthetic treatments. These advances have triggered the development of myriad neural technologies to design multimodal neural implants (*2*–*5*). However, the conversion of these sophisticated technologies into implants mediating long-lasting therapeutic benefits has yet to be achieved. A recurring challenge restricting long-term biointegration is the substantial biomechanical mismatch between implants and neural tissues (*6*–*8*). Neural tissues are viscoelastic (*9*, *10*) with elastic and shear moduli in the 100- to 1500-kPa range. They are mechanically heterogeneous (*11*, *12*) and endure constant body dynamics (*13*, *14*). In contrast, most electrode implants—even thin, plastic interfaces—present high elastic moduli in the gigapascal range, thus are rigid compared to neural tissues (*3*, *15*). Consequently, their surgical insertion triggers both acute and long-term tissue responses (*6*–*8*, *14*). Here, we tested the hypothesis that neural implants with mechanical properties matching the statics and dynamics of host tissues will display long-term biointegration and functionality within the brain and spinal cord.

We designed and engineered soft neural interfaces that mimic the shape and mechanical behavior of the dura mater (Fig. 1, A and B, and fig. S1). The implant, which we called electronic dura mater or e-dura, integrates a transparent silicone substrate (120 μm in thickness), stretchable gold interconnects (35 nm in thickness), soft electrodes coated with a platinum-silicone composite (300 μm in diameter), and a compliant fluidic microchannel (100 μm by 50 μm in cross section) (Fig. 1, C and D, and figs. S2 to S4). The interconnects and electrodes transmit electrical excitation and transfer electrophysiological signals. The microfluidic channel, termed chemotrode (*16*), delivers drugs locally (Fig. 1C and fig. S4). The substrate, encapsulation, and microchannel silicone layers are prepared with soft lithography and assembled by covalent bonding following oxygen plasma activation (Fig. 1D and fig. S2). Interconnects are thermally evaporated through a stencil mask, whereas electrodes are coated with the soft composite by screen-printing (fig. S2). Microcracks in the gold interconnects (*17*) and soft platinum-silicone composite electrodes confer exceptional stretchability to the entire implant (Fig. 1D and movie S1).

Most implants used experimentally or clinically to assess and treat neurological disorders are placed above the dura mater (*15*, *18*–*20*). The compliance of the soft implant enables surgical insertion below the dura mater through a small opening (Fig. 1, A and C, and fig. S5). This location provides an intimate interface between electrodes and targeted neural tissues (Fig. 1E) and allows direct delivery of drugs into the intrathecal space. To illustrate these properties, we fabricated implants tailored to the spinal cord, one of the most demanding environments of the central nervous system. We developed a vertebral orthosis to secure the connector (Fig. 1F) and dedicated surgical procedures for subdural implantation (fig. S5). The soft implant smoothly integrated the subdural space along the entire extent of lumbosacral segments (2.5 cm in length and 0.3 cm in width), conforming to the delicate spinal neural tissue (Fig. 1, E and F).

We next tested the long-term biointegration of soft implants compared to stiff, plastic implants (6 weeks of implantation). A stiff implant was fabricated by means of a 25-μm-thick polyimide film, which corresponds to standard practices for flexible neural implants (*21*) and is robust enough to withstand the surgical procedure. Both types of implants were inserted into the subdural space of lumbosacral segments in healthy rats. A sham-operated group of animals received the headstage, connector, and vertebral orthosis but without spinal implant.

To assess motor performance, we obtained high-resolution kinematic recordings of whole-body movement during basic walking and skilled locomotion across a horizontal ladder. In the chronic stages, the behavior of rats with soft implants was indistinguishable from that of sham-operated animals (Fig. 2A, fig. S6, and movie S2). By contrast, rats with stiff implants displayed significant motor deficits that emerged around 1 to 2 weeks after implantation and deteriorated over time. They failed to accurately position their paws onto the rungs of the ladder (Fig. 2A). Even during basic walking, rats with stiff implants showed pronounced gait impairments, including altered foot control, reduced leg movement, and postural imbalance (fig. S6).

The spinal cords were explanted after 6 weeks of implantation. Both soft and stiff implants occupied the targeted location within the subdural space. Minimal connective tissue was observed around the implants. To evaluate potential macroscopic damage to the spinal cord that may explain motor deficits, we reconstructed the explanted lumbosacral segments in three dimensions. A

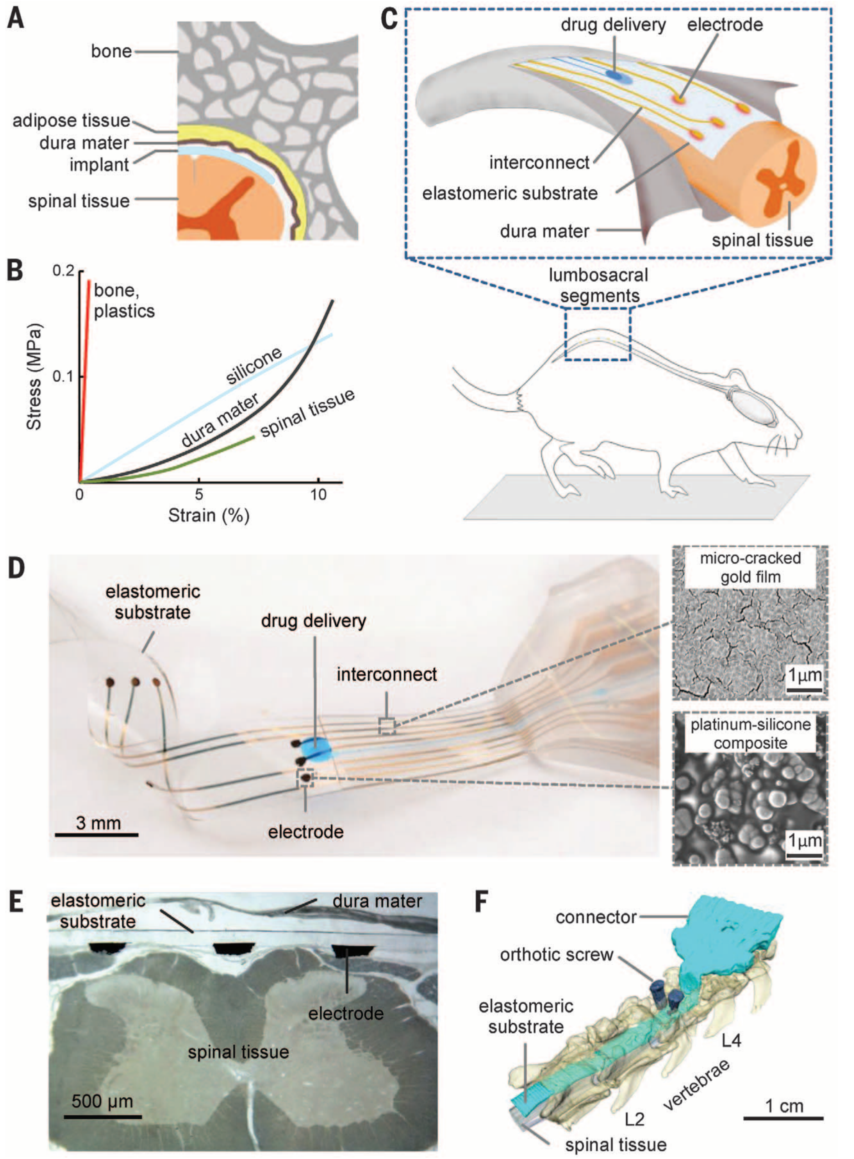

Fig. 1. Electronic dura mater, "e-dura," tailored for the spinal cord. (**A**) Schematic cross section of the vertebral column with the soft implant inserted in the spinal subdural space. (**B**) Strain-stress curves of spinal tissues, dura mater, and implant materials. Plastics (polyimide), silicone, and dura mater responses are experimental data. Spinal tissue response is adapted from the literature (see supplementary materials). (**C**) Illustration of the e-dura implant inserted in the spinal subdural space of rats. (**D**) Optical image of an implant, and scanning electron micrographs of the gold film and the platinum-silicone composite. (**E**) Cross-section of an e-dura inserted for 6 weeks in the spinal subdural space. (**F**) Reconstructed 3D micro–computed tomography scans of the e-dura inserted in the spinal subdural space covering L2 to S1 spinal segments in rats. The scan was obtained in vivo at week 5 after implantation.

---

[1]Bertarelli Foundation Chair in Neuroprosthetic Technology, Laboratory for Soft Bioelectronic Interfaces, Centre for Neuroprosthetics, Institute of Microengineering and Institute of Bioengineering, Ecole Polytechnique Fédérale de Lausanne (EPFL), Switzerland. [2]International Paraplegic Foundation Chair in Spinal Cord Repair, Centre for Neuroprosthetics and Brain Mind Institute, EPFL, Switzerland. [3]Pavlov Institute of Physiology, St. Petersburg, Russia. [4]Translational Neural Engineering Laboratory, Center for Neuroprosthetics and Institute of Bioengineering, EPFL, Lausanne, Switzerland. [5]School of Engineering and Applied Sciences, Kavli Institute for Bionano Science and Technology, Harvard University, Cambridge, MA, USA. [6]Laboratory for Biosensors and Bioelectronics, Institute for Biomedical Engineering, University and ETH Zurich, Switzerland. [7]The BioRobotics Institute, Scuola Superiore Sant'Anna, Pisa 56025, Italy.
*These authors contributed equally to this work. †These authors contributed equally to this work. ‡**Corresponding author. E-mail: gregoire.courtine@epfl.ch (G.C.); stephanie.lacour@epfl.ch (S.P.L.)**

cross-sectional circularity index was calculated to quantify changes in shape. All the rats with stiff implants displayed significant deformation of spinal segments under the implant ($P < 0.05$, Fig. 2B), ranging from moderate to extreme compression (fig. S7 and movie S2).

Neuroinflammatory responses at chronic stages were visualized with antibodies against activated astrocytes and microglia (Fig. 2C), two standard cellular markers for foreign-body reaction (*7*). As anticipated from macroscopic damage, both cell types massively accumulated in the vicinity of stiff implants ($P < 0.05$; Fig. 2C and fig. S8). In marked contrast, no significant difference was found between rats with soft implants and sham-operated animals (Fig. 2C and fig. S8). These results demonstrate the long-term biocompatibility of the soft implants.

We manufactured a model of spinal cord using a hydrogel core to simulate spinal tissues and a silicone tube to simulate the dura mater (fig. S9A). A soft or stiff implant was inserted into the model (Fig. 2D). The stiff implant induced a pronounced flattening of the simulated spinal cord, whereas the soft implant did not alter the circularity of the model (Fig. 2D and fig. S10). To provide the model with realistic metrics, we quantified the natural flexure of the spine in freely moving rats (fig. S9B). When the model was bent, the stiff implant formed wrinkles that induced local compressions along the hydrogel core. In contrast, the soft implant did not affect the smoothness of simulated spinal tissues (fig. S11). When the model was stretched, the stiff implant slid relative to the hydrogel core, whereas the soft implant elongated together with the entire spinal cord (Fig. 2D and fig. S11). Reducing the thickness of the plastic implant to 2.5 μm improved bending stiffness and conformability. However, the ultrathin, plastic implant still failed to deform during motion of the soft tissue (fig. S10 and supplementary text).

Patterning extremely thin films into web-like systems offers alternative mechanical designs for elastic surfaces (*22*–*24*). For example, fractal-like meshes develop into out-of-plane structures during mechanical loading, which facilitates reversible and local compliance. Medical devices prepared with such three-dimensional (3D) topologies can conform the curvilinear surface of the heart (*25*) and skin (*23*). However, this type of interface requires complex, multistep processing and transient packaging. In comparison, fabrication steps of e-dura are remarkably simple. Moreover, the shape and unusual resilience of the soft implant greatly facilitate surgical procedures.

The composite electrodes of the soft implant displayed low impedance ($Z = 5.2 \pm 0.8$ kilohm at 1 kHz, $n = 28$ electrodes) and maintained the electrochemical characteristics of platinum (Fig. 3,

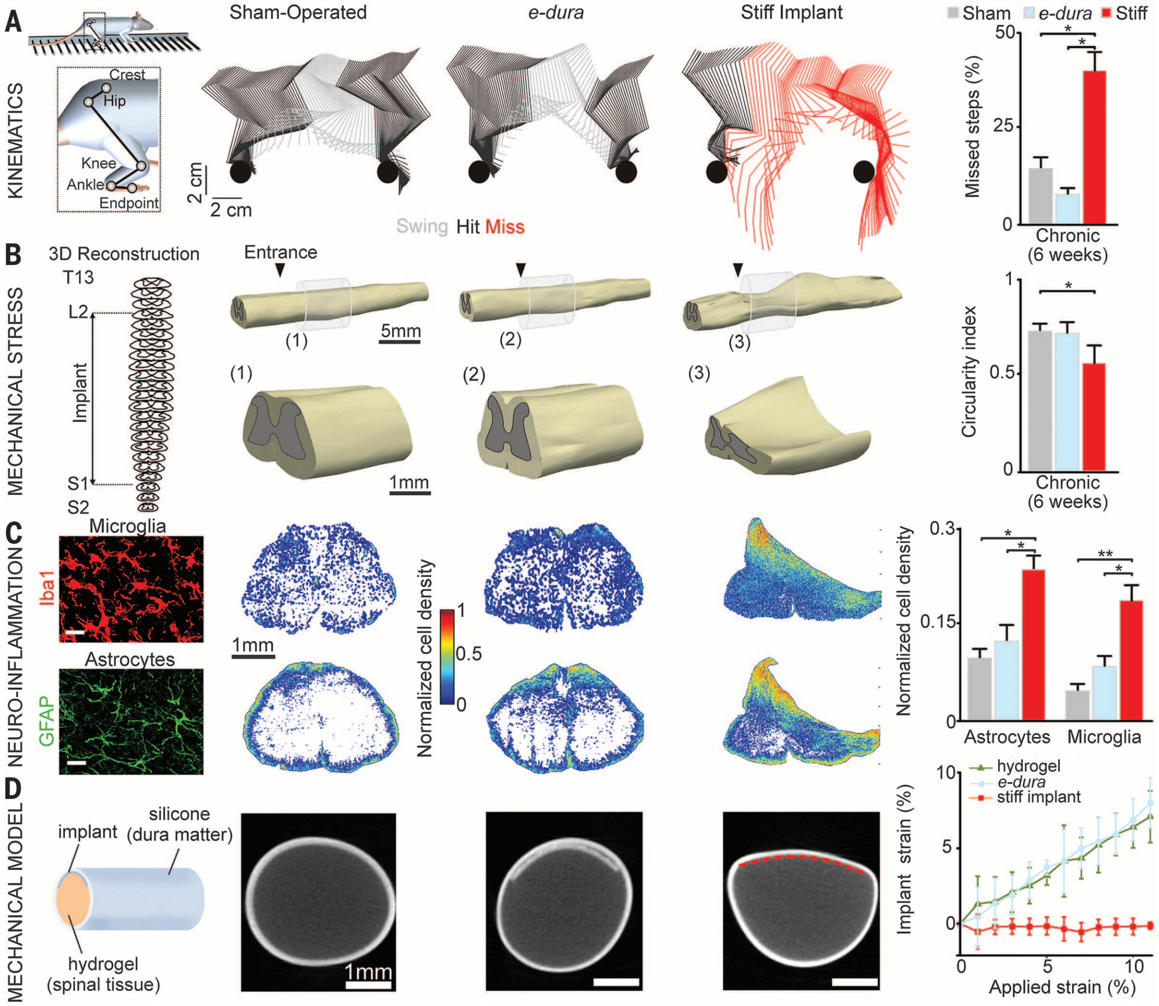

Fig. 2. Biointegration. (**A**) Hindlimb kinematics during ladder walking 6 weeks after implantation. Bar plots reporting mean percentage of missed steps averaged per animal onto the rungs of the ladder ($n = 8$ trials per rat, $n = 4$ rats per group). (**B**) 3D spinal cord reconstructions, including enhanced views, 6 weeks after implantation. The arrowheads indicate the entrance of the implant into the subdural space. Bar plots reporting mean values of spinal cord circularity index ($4\pi \times \text{area/perimeter}^2$). (**C**) Photographs showing microglia (Iba1) and astrocytes (GFAP, glial fibrillary acidic protein) staining reflecting neuroinflammation. Scale bars: 30μm. Heat maps and bar plots showing normalized astrocyte and microglia density. (**D**) Spinal cord model scanned using micro–computed tomography without and with a soft or stiff implant. e-dura implant is 120 μm thick. The red line materializes the stiff implant (25 μm thick), not visualized because of scanner resolution. Plot reporting local longitudinal strain as a function of global applied strain. Statistical test: Kruskal-Wallis one-way analysis of variance (*$P < 0.05$; **$P < 0.01$. Error bars: SEM).

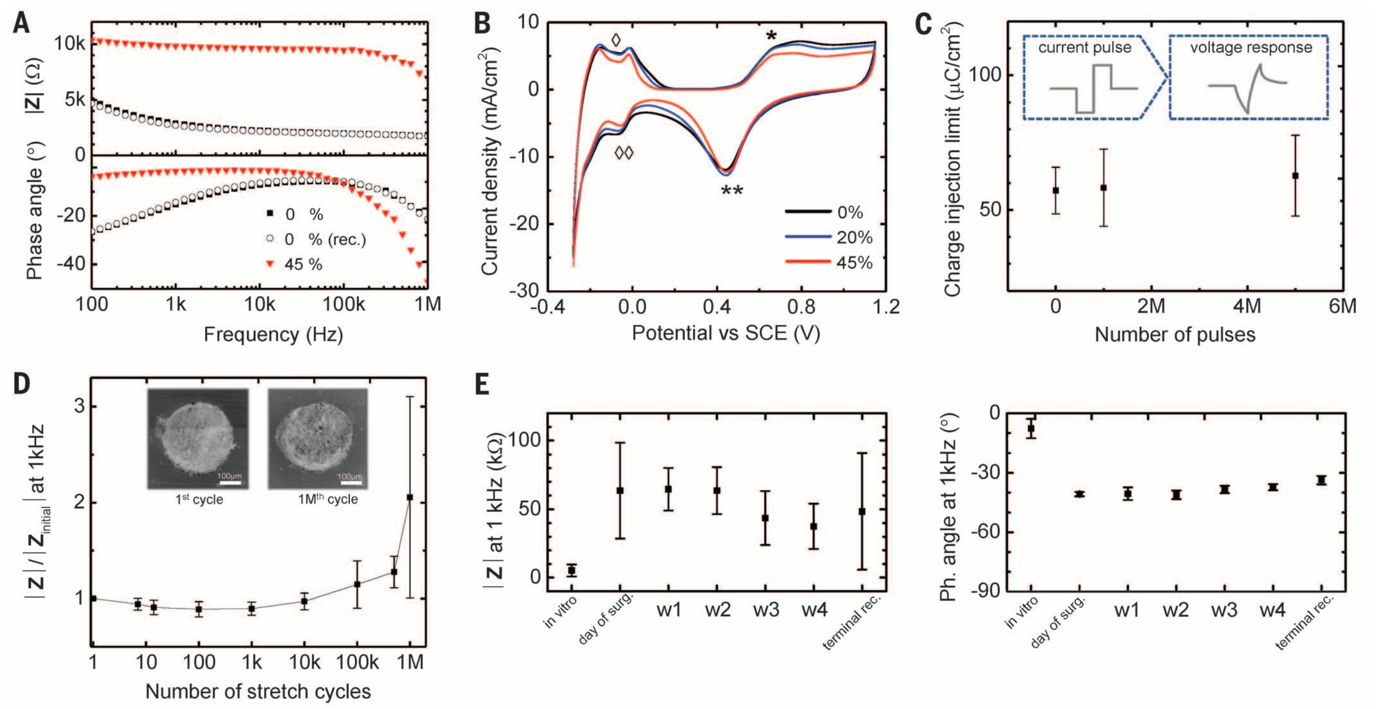

Fig. 3. Properties of e-dura electrodes. (**A**) Magnitude and phase of electrode impedance recorded in saline solution (pH 7.4). Spectra were collected before (■), at maximum elongation (▼), and after (○) a uniaxial stretch cycle to 45% strain. (**B**) Cyclic voltammograms recorded in diluted sulfuric acid (pH 0.9) during a uniaxial stretch cycle to 45% strain. Cyclic voltammetry (50 mV/s) reveals high current densities through the electrode even at large strain. Peaks correspond to oxide formation (*), oxide reduction (**), H$^+$ adsorption (◊◊), and H$^+$ desorption (◊) on Pt metal surfaces. (**C**) Charge injection limit of electrodes ($n = 4$, mean ±SD) and evolution after repeated pulsing. (**D**) Relative impedance modulus of electrodes ($n = 7$, mean ± SD) at 1kHz and at rest and after uniaxial fatigue cycling to 20% strain. Inset: scanning electron micrographs of an electrode after the first and one millionth stretch cycles. (**E**) Modulus and phase at 1 kHz ($n = 28$ total electrodes, mean ± SD, across four rats) recorded in vitro, then in vivo immediately after implantation and weekly until terminal procedure.

A and B). Cyclic voltammograms of the composite electrodes remained unchanged when the implant was stretched up to a strain of 45%. The high effective surface area of the platinum-silicone composite produced a large cathodal charge storage capacity of 46.9 ± 3.3 mC/cm^2. This value is two orders of magnitude higher than that of smooth platinum (*26*) and is smaller but comparable to that of highly doped organic electrode coatings (*27*). The composite electrode supported a charge injection limit of 57 ± 9 μC/cm^2, which is comparable to the injection limit of platinum (*26*) (Fig. 3C and fig. S12). These characteristics remained stable even after 5 million electrical pulses, which corresponds to more than 30 hours of continuous stimulation with clinically relevant parameters (40 Hz, charge-balanced, biphasic, 100-μA current pulse, 0.2-ms pulse width).

To demonstrate the robustness of the soft implant against deformation experienced by natural dura mater during daily living activities, we stretched the device to 20% strain over 1 million cycles. The implant, the chemotrode, and the seven embedded electrodes withstood the cyclic deformation, displaying minimal variation in impedance over time (Fig. 3D, figs. S13 and S14, and movie S1). Assuming radical postural changes approximately every 5 min, these results indicate that the soft implant would survive mechanically for nearly a decade in a patient.

Electrode impedance and chemotrode functionality were evaluated over 5 weeks in four rats (n = 28 electrodes and 4 chemotrodes in total). Impedance at 1 kHz remained constant throughout the 5 weeks of implantation (Fig. 3E), demonstrating stability of stretchable electrodes in vivo. Daily injections of drugs and hydrodynamic evaluations of microfluidic channels after explantation (fig. S4) confirmed that the chemotrodes remain operational for extended durations in vivo.

These combined results demonstrate electrochemical stability, mechanical robustness, and long-term functionality of the soft electrodes and chemotrodes, fulfilling the challenging requirements for long-term implantation.

We exploited the soft neurotechnology to tailor electronic dura mater for the brain and spinal cord. An e-dura, consisting of a 3 × 3 electrode array, was placed over the motor cortex of mice expressing the light-sensitive channel channelrhodopsin-2 in the majority of neurons (Fig. 4A). The silicone substrate is optically transparent, enabling concurrent optical stimulation and neural recording. The cortical surface was illuminated with a laser focused on distinct locations to activate neurons locally. The spatial resolution of electrocorticograms recorded from the e-dura allowed extraction of neuronal activation maps that were specific for each site of stimulation (Fig. 4A).

An e-dura was then inserted between the dura mater and motor cortex tissues (fig. S5) to record electrocorticograms in conjunction with whole-body kinematic, and leg muscle activity in freely moving rats (Fig. 4B). Power spectral density analysis applied on electrocorticograms (*28*) identified standing and locomotor states over several weeks of recordings (Fig. 4B and fig. S15). To verify whether neural recordings could also be obtained from an e-dura chronically implanted over spinal tissues, we measured electrospinograms in response to electrical stimulation of the motor cortex or the sciatic nerve. Descending motor command was reliably recorded (fig. S16), and peripheral sensory feedback was detected with notable spatial and temporal selectivity after 6 weeks of implantation (Fig. 4C and fig. S16).

We finally exploited the e-dura to restore locomotion after spinal cord injury (*4*, *19*). Adult rats received a clinically relevant contusion at the thoracic level, which spared less than 10% of spinal tissues at the lesion epicenter and led to permanent paralysis of both legs (Fig. 4D). An e-dura covering lumbosacral segments (Fig. 1) was used to engage spinal locomotor circuits located below injury. A serotonergic replacement therapy ($5HT_{1A/7}$ and $5HT_2$ agonists) (*29*) was injected through the chemotrode, and continuous electrical stimulation was delivered on the lateral aspect of L2 and S1 segments (40 Hz, 0.2 ms, 50 to 150 μA) (*30*). The concurrent and colocalized electrical and chemical stimulations enabled the paralyzed rats to walk (Fig. 4E). Intrathecal delivery allowed a reduction of injected drug volume to one-quarter the volume of intraperitoneal injection required to obtain the same facilitation of stepping (fig. S17). Subdural drug delivery through the chemotrode eliminated side effects of serotonergic

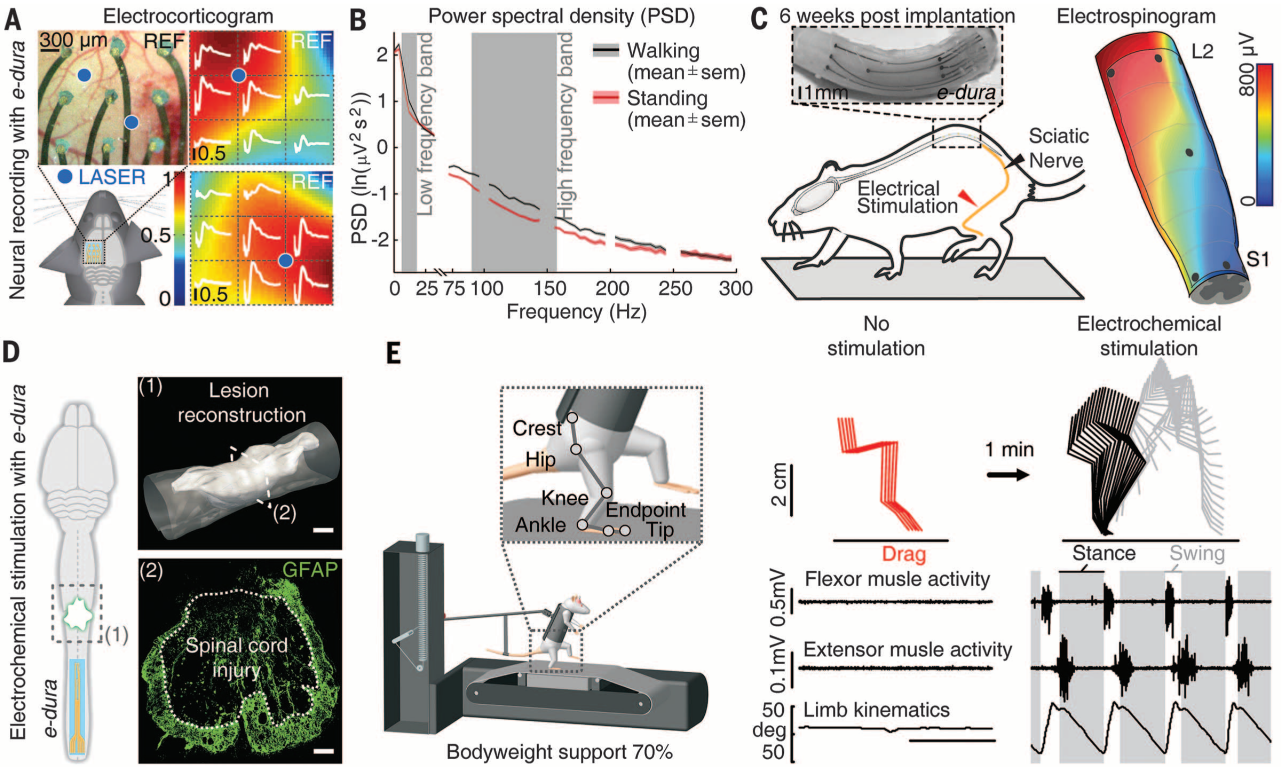

Fig. 4. Recordings and stimulation with e-dura. (**A**) e-dura implant positioned over the cortical surface of a Thy1-ChR2-YFP (yellow fluorescent protein) mouse. Blue spot indicates laser location. Cortical activation maps were reconstructed from normalized electrocorticograms, shown in white (150-µs duration). (**B**) Power spectral density computed from motor cortex electrocorticograms recorded 3 weeks after e-dura implantation in rats. Increased neural activity in low- and high-frequency bands differentiate cortical states during walking from those during standing. (**C**) Spinal cord activation map was reconstructed from electrospinograms recorded 6 weeks after e-dura implantation in response to left sciatic nerve stimulation. (**D**) Rats were implanted with a spinal e-dura covering lumbosacral segments and received a severe spinal cord injury. (**E**) Recording without and with electrochemical stimulation during bipedal locomotion under robotic support after 3 weeks of rehabilitation. Stick diagram decompositions of hindlimb movements are shown together with leg muscle activity and hindlimb oscillations.

agents on autonomic systems (fig. S17). The distributed electrodes delivered stimulation restricted to specific segments, which allowed facilitation of left versus right leg movements (fig. S18 and movie S3). The e-dura mediated reliable therapeutic effects during the 6-week rehabilitation period.

We have introduced soft neural implants that show long-term biointegration and functionality within the central nervous system. Computerized and mechanical simulations demonstrated that the biomechanical coupling between implants and neural tissues is critical to obtain this symbiosis. Neural implants prepared with elastic materials met the demanding static and dynamic mechanical properties of spinal and brain tissues. Even in the subdural space, the soft implant triggered limited foreign-body reaction. This location enables local drug application, reducing side effects; high-resolution neuronal recordings; and concurrent delivery of electrical and chemical neuromodulation, alleviating neurological deficits for extended periods of time. The integration of tissue-matched implants with higher electrode density, implantable pumps for drug delivery, and embedded electronics to read and write into the nervous system in real time will require additional technological developments.

REFERENCES AND NOTES

1. D. Borton, S. Micera, J. R. Millán, G. Courtine, *Sci. Transl. Med.* **5**, 210rv2 (2013).
2. D.-H. Kim *et al.*, *Nat. Mater.* **9**, 511–517 (2010).
3. P. Fattahi, G. Yang, G. Kim, M. R. Abidian, *Adv. Mater.* **26**, 1846–1885 (2014).
4. R. van den Brand *et al.*, *Science* **336**, 1182–1185 (2012).
5. D. W. Park *et al.*, *Nat. Commun.* **5**, 5258 (2014).
6. J. C. Barrese *et al.*, *J. Neural Eng.* **10**, 066014 (2013).
7. P. Moshayedi *et al.*, *Biomaterials* **35**, 3919–3925 (2014).
8. K. A. Potter *et al.*, *Acta Biomater.* **10**, 2209–2222 (2014).
9. Y.-B. Lu *et al.*, *Proc. Natl. Acad. Sci. U.S.A.* **103**, 17759–1776 (2006).
10. B. S. Elkin, A. I. Ilankovan, B. Morrison 3rd, *J. Neurotrauma* **28**, 2235–2244 (2011).
11. A. F. Christ *et al.*, *J. Biomech.* **43**, 2986–2992 (2010).
12. B. S. Elkin, E. U. Azeloglu, K. D. Costa, B. Morrison 3rd, *J. Neurotrauma* **24**, 812–822 (2007).
13. D. R. Enzmann, N. J. Pelc, *Radiology* **185**, 653–660 (1992).
14. D. E. Harrison, R. Cailliet, D. D. Harrison, S. J. Troyanovich, S. O. Harrison, *J. Manipulative Physiol. Ther.* **22**, 227–234 (1999).
15. P. Konrad, T. Shanks, *Neurobiol. Dis.* **38**, 369–375 (2010).
16. P. Musienko, R. van den Brand, O. Maerzendorfer, A. Larmagnac, G. Courtine, *IEEE Trans. Biomed. Eng.* **56**, 2707–2711 (2009).
17. S. P. Lacour, D. Chan, S. Wagner, T. Li, Z. Suo, *Appl. Phys. Lett.* **88**, 204103 (2006).
18. A. Mailis-Gagnon, A. D. Furlan, J. A. Sandoval, R. Taylor, *Cochrane Database Syst. Rev.* (3): CD003783 (2004).
19. C. A. Angeli, V. R. Edgerton, Y. P. Gerasimenko, S. J. Harkema, *Brain* **137**, 1394–1409 (2014).
20. P. Gad *et al.*, *J. Neuroeng. Rehabil.* **10**, 2 (2013).
21. NeuroNexus, Surface Probes. http://neuronexus.com/products/neural-probes/surface-probes, (2014).
22. C. F. Guo, T. Sun, Q. Liu, Z. Suo, Z. Ren, *Nat. Commun.* **5**, 3121 (2014).
23. J. A. Fan *et al.*, *Nat. Commun.* **5**, 3266 (2014).
24. J. Vanfleteren *et al.*, *Procedia Technol.* **15**, 208–215 (2014).
25. D.-H. Kim *et al.*, *Proc. Natl. Acad. Sci. U.S.A.* **109**, 19910–19915 (2012).
26. S. F. Cogan, *Annu. Rev. Biomed. Eng.* **10**, 275–309 (2008).
27. U. A. Aregueta-Robles, A. J. Woolley, L. A. Poole-Warren, N. H. Lovell, R. A. Green, *Front. Neuroeng.* **7**, 15 (2014).
28. T. Pistohl, A. Schulze-Bonhage, A. Aertsen, C. Mehring, T. Ball, *Neuroimage* **59**, 248–260 (2012).
29. P. Musienko *et al.*, *J. Neurosci.* **31**, 9264–9278 (2011).
30. G. Courtine *et al.*, *Nat. Neurosci.* **12**, 1333–1342 (2009).

ACKNOWLEDGMENTS

We thank D. Pioletti for providing access to the micro–computed tomography (CT) scanner. Financial support was provided by the Fondation Bertarelli, the International Paraplegic Foundation, Starting Grants from the European Research Council (ERC 259419 *ESKIN* and ERC 261247 *Walk-Again*), Nano-tera.ch (20NA_145923 *SpineRepair*), the Swiss National Science Foundation through the National Centre of Competence in Research (NCCR) in Robotics, European Commission's Seven Framework Program (CP-IP 258654 *NeuWalk*), and the National Science Foundation Materials Research Science and Engineering Center (DMR-0820484). A patent application (PCT/EP2014/059779) describing aspects of the implant fabrication was filed on 13 May 2014.

SUPPLEMENTARY MATERIALS

www.sciencemag.org/content/347/6218/159/suppl/DC1
Materials and Methods
Supplementary Text
Table S1
Figs. S1 to S18
Movies S1 to S3
References (*31*, *32*)

22 August 2014; accepted 27 November 2014
10.1126/science.1260318